Published by IOP Publishing for Sissa Medialab

Received: *October 31, 2024*
Accepted: *January 2, 2025*
Published: *February 12, 2025*

25th International Workshop on Radiation Imaging Detectors
Lisbon, Portugal
30 June – 4 July 2024

Solid angle compensation in gas proportional scintillation counters using an annular anode with azimuthal geometry

P.A.O.C. Silva,* **L.M.P. Fernandes**, **J.M.F. dos Santos** and **C.M.B. Monteiro***

LIBPhys, Physics Department, University of Coimbra,
P-3004-516 Coimbra, Portugal

E-mail: cristinam@uc.pt, pesilva@uc.pt

Abstract: A new, simple and robust design for a gas proportional scintillation counter (GPSC) is studied. One sole electrode, the anode, is used to define the electric field in the drift and scintillation regions of the detector volume. The anode has an annular shape aligned with the photosensor axis. Such design allows to keep constant the solid angle subtended by the photosensor relative to the different positions of the scintillation region. Having an oblong anode with a 10 cm inner diameter and a 5 cm photomultiplier tube placed 5 cm below the anode, an energy resolution of 12.0 % FWHM has been achieved for a 10 kV anode bias, the maximum voltage that could be applied to the anode in the present prototype. According to simulations, energy resolutions of ~10 % can be achieved for anode voltages of ~13 kV, a value comparable to the 9–10 % achieved in GPSC using solid angle variation compensation. Independently of having a constant solid angle, the absolute value of the solid angle must be considered, a lower number of EL photons detected at the photosensor due to a reduced solid angle may contribute to the GPSC energy resolution degradation. In addition, non-uniformities present in the photosensor or in the GPSC must be taken into account, since they will contribute to a dependence of the pulse amplitude on the radiation interaction position despite the constant solid angle subtended by the photosensor relative to the scintillation region.

Keywords: Charge transport, multiplication and electroluminescence in rare gases and liquids; Detector design and construction technologies and materials; Detector modelling and simulations II (electric fields, charge transport, multiplication and induction, pulse formation, electron emission, etc); Gaseous detectors

---

*Corresponding author.

https://doi.org/10.1088/1748-0221/20/02/C02021

2025 JINST 20 C02021

Contents

1 Introduction

Large area and large volume xenon-based radiation detectors have been used for x-ray and γ-ray spectrometry in applications such as x-ray fluorescence analysis, x-ray astrophysics, asteroid and planetary surveys [1–11]. Xenon is an attractive medium for x- and γ-ray detection featuring large stopping power, high ionization and scintillation yields and good energy resolution. Solid state detectors are actively used since they feature higher stopping power, high position resolution, response speed, and lifetime. Nevertheless, xenon gaseous detectors present advantages such as its stability for long term missions, high resistance to radiation damage, wide range of operating temperatures, simplicity and flexibility for designing detectors. In addition, gaseous detectors are advantageous when high detection areas are needed.

An important feature of noble gas detectors is the possibility to obtain the primary ionization signal amplification by promoting secondary scintillation in the gas through electron impact, the so-called electroluminescence (EL). The primary ionization electrons drift through the gas, under an electric field below the excitation threshold, into a specific region where the electric field is strong enough to excite but not ionize the atoms, producing EL upon the atoms de-excitation. In opposition to the signal amplification through charge avalanche processes and subsequent charge readout, the statistical fluctuations associated to the EL process and respective photon readout can be made much lower than the intrinsic statistical fluctuations associated to the primary electron cloud formation, related to the Fano factor.

However, the dependency of the solid angle subtended by the photosensor relative to the EL emission position, consequently, on the radiation interaction position, introduces additional fluctuations in the detected scintillation, limiting the size of the detector radiation window relative to that of the photosensor active area. Different solutions have been proposed to mitigate this effect. Focusing the primary ionization electrons into the region around the photosensor axis [2–4, 10] allowed to build gas proportional scintillation counters (GPSCs) with a GPSC window-to-PMT diameter ratio of about 2.5. Alternatively to multi-electrode focusing of primary electrons in the drift region, other techniques such as radially increasing the electric field in the scintillation region or else radially decreasing the transmission of a mask placed on top of the PMT window [5–7] in such a way that the radial decrease of the solid angle is compensated. These procedures reduce the cost and the complexity of the focusing technique although limiting the GPSC window-to-PMT diameter ratio to ~0.8 [6].

To minimize the solid angle variations in a GPSC, we recently proposed a different and quite simpler GPSC design [12], having a single electrode, the anode, with an annular shape with its axis aligned with the photosensor axis. Biased at high voltage, the anode defines the electric field in both the drift and the scintillation regions. The electric field intensity decreases with increasing distance to the anode, being the scintillation region located around the anode where the electric field intensity is above the gas scintillation threshold, and the drift region the remaining detector volume. In this design, the entire scintillation region has the same solid angle subtended by the photosensor and the EL light detected in the photosensor will be independent from the x-ray interaction position. To avoid scintillation shadowing by the anode, only a tip of the anode is in contact with the gas volume, being most of the anode hidden inside the inner wall of the detector, made from an insulating material [12]. The proof-of-concept has been presented in [12]. An energy resolution of 14% FWHM for 5.9 keV x-rays have been achieved for a maximum anode voltage of 8 kV bias, an oblong disk of with 98 mm (106 mm) internal (external) diameter having a 2 mm section radius and being the scintillation readout by a 5 cm diameter PMT. This value is still far from the 9–10% energy resolution obtained by the geometries using solid angle compensation. Nevertheless, it was shown that there was room for improvements.

In this work, the performance of an improved version of such GPSC is studied and the obtained results are discussed. Simulation studies, using state-of-art software for the primary charge generation, electron drift and diffusion, photon emission due to the increasing electric field, light propagation and collection in the photosensor, are also presented.

2 Experimental setup

The schematic of the annular anode GPSC is depicted in figure 1. It is the same as that of [12], except for the inner wall insulator, which is made, now, out of HDPE covered by a 2-mm thick PTFE, substituting PEEK. This change had two advantages: it allowed achieving higher biasing voltage applied to the anode and it improved scintillation collection efficiency due to the higher PTFE VUV reflectivity. Both the HDPE and the PTFE were perforated to allow for gas circulation.

The anode is made of 4-mm thick stainless-steel, oblong shaped disk with 96 mm (106 mm) internal (external) diameter, having a 2 mm radius section at the edges. The inner wall of the chamber is made from PTFE, having an inner diameter of 98 mm. The detector chamber is a stainless-steel cylinder, 150 mm in diameter and 100 mm long. The GPSC radiation window is 100 mm in diameter, 125 µm thick Kapton foil aluminized on the inner surface, epoxied to a stainless-steel disk. The lower base plate is a stainless-steel disk, epoxied to a Macor piece, which is also epoxied to a 5-cm in diameter photomultiplier tube (PMT) having its window facing the gas volume.

The gas inlet and outlet flanges are connected to a U-shape tubing having one of its vertical tubes filled with non-evaporable getters [26], kept at 250 °C, promoting gas circulation by convection for continuous gas purification. The GPSC is filled with xenon at a pressure of 1.1 bar. For the studies of the GPSC-to-photosensor window diameter ratios above 2, the PMT was substituted by a 16 mm active area large-area avalanche photodiode (LAAPD) [13] as the photosensor.

Radiation interactions occurring in the detector volume produce a primary electron cloud that drift towards the anode leading to an EL pulse, read by the photosensor. The photosensor is connected thorough a pre-amplifier and an amplifier, with a 4-µs shaping time, to a multi-channel analyser to record the pulse-height distributions.

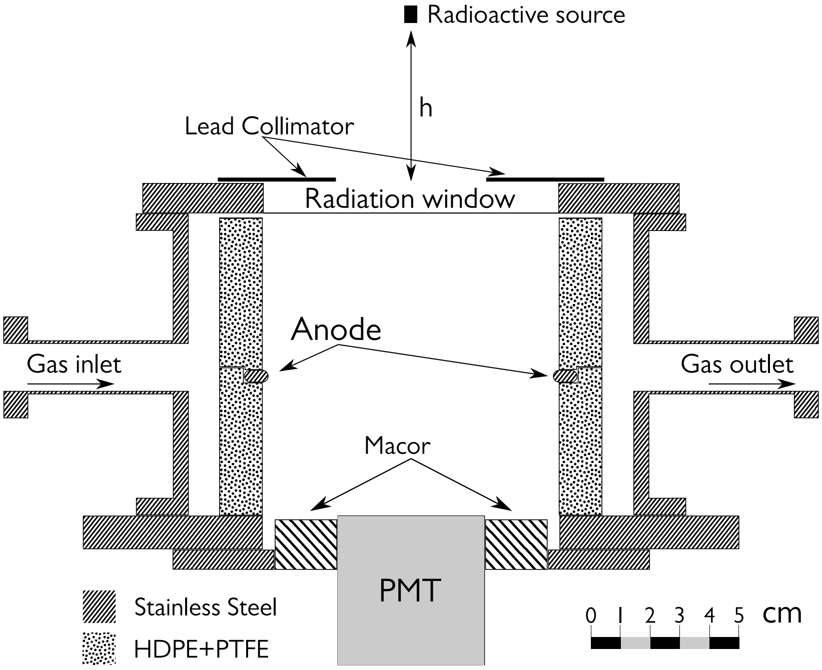

Figure 1. Schematic of the annular anode GPSC.

3 Simulations

To access the electric field in the detector volume a combination of three packages was used. Salome platform [14] was used to define the geometry and mesh of the different detector components and the relevant boundaries for the simulation. This mesh was imported to Elmer-FEM [15] to calculate the electric field. Paraview [16] was used to inspect and export the simulation results. Except for a very small volume at the centre of the anode ring, the reduced electric field is above 0.1 $\mathrm{kV{\cdot}cm^{-1}{\cdot}bar^{-1}}$ throughout the whole gas volume, hence high enough to prevent electron-ion recombination in the ionization tracks resulting from the radiation interaction. The scintillation region remains within 1.5 cm from the anode, where the reduced electric field is above the xenon scintillation threshold, 0.8 $\mathrm{kV{\cdot}cm^{-1}{\cdot}bar^{-1}}$ [17]. Nevertheless, most of the EL takes place in the vicinity of the anode surface due to the radial dependence of the electric field in the region around the anode.

Independent simulations were performed for 5.9-, 22.1- and 59.54-keV photons. Using GEANT4 [18–20], the photons were generated at a given distance above the collimator and emitted isotropically. The interaction position of each photon interacting inside the gas volume was recorded. For each photon absorption position, the positions of the electrons of the respective primary electron cloud were determined using the DEGRAD framework [21], considering the experimental conditions, electric field, pressure and temperature (296 °K). A random sample of electrons was taken from each primary electron cloud and the Garfield++ [22] framework was used to drift each sampled electron from its initial position towards the anode, using the electric field map obtained from Elmer-FEM. From Garfield++, the Xe excitations and ionizations positions were obtained along each electron drift path. From these positions, a Xe VUV photon was isotropically emitted and followed, using a GEANT4 optical framework [18–20], which includes the detailed geometry and all the materials of the detector chamber. VUV reflections in the inner surfaces of the chamber were taken into account,

2025 JINST 20 C02021

assuming the reflectivity values found in the literature. Therefore, the average number of VUV photons and respective statistical fluctuations produced per primary electron and/or per x- or γ-ray interaction, as well as the average number of VUV impinging the photosensor active area, can be estimated. For a 10 kV bias of the anode, an average number of 530 EL photons are produced per primary electron. This value is similar to that achieved in Xe at 1.1 bar and in a 1 cm thick uniform electric field configuration with a reduced electric field close to the charge multiplication threshold, 4.5 kV·cm^{-1}·bar^{-1} [17].

4 Results and discussion

Typical pulse-height distributions obtained for 5.9-keV x-rays and for the x- and γ-photons from a ^{109}Cd and ^{241}Am radioactive sources are presented in figure 2, for a 10 kV anode biasing voltage. The spectra exhibit the advantages of the EL amplification, the low amplitude of the background noise tail at the low energy limit is lower than few hundred eV, denoting a very high signal-to-noise ratio. In addition, the low level of the background plateau denotes the negligible effect of the electron-ion recombination and/or the electron loss due to attachment during the drift towards the anode. The high background plateau of the ^{241}Am spectrum is due to pile-up.

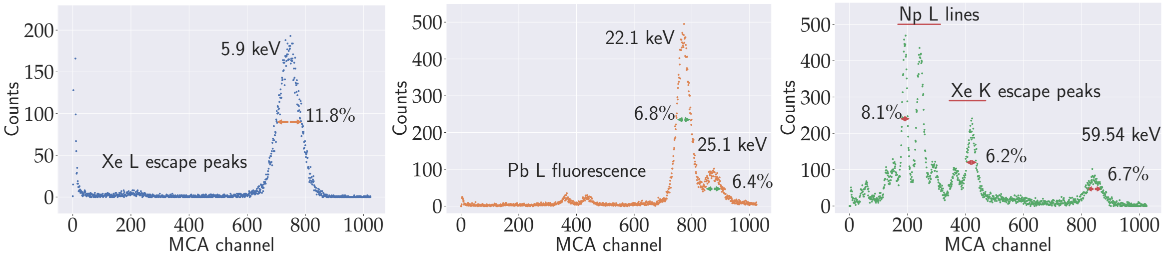

Figure 2. Pulse-height distribution for 5.9-keV x-rays and for the x- and γ-photons from a ^{109}Cd and an ^{241}Am radioactive sources.

From the ^{241}Am spectrum, we plot the pulse amplitude as a function of the energy deposition in the gas, figure 3a). The amplitude trend exhibits the expected good energy linearity of the GPSC. However, the obtained energy resolutions are still worse than those obtained in xenon-filled GPSCs with other geometries [2, 4, 6]. Figure 3b) depicts the square of the energy resolution as a function of the reciprocal of the energy (1/E), for the 5.9, 14.0, 22.1, 25.1 and 29.7 keV lines. The stochastic term follows the $1/\sqrt{E}$ dependence being the constant term an energy independent systematic contribution, denoting the presence of detector specific systematic effects, e.g. such as non-uniformities related to the photosensor or to the detector chamber. The contribution of this term is rather high, 3.6 % FWHM, presenting the limit energy resolution that can be obtained in our detector for very high energies. The deviation of the energy resolution from the linear trend for high energies is due to the greater range in the absorption depths and to the dimension of the primary electron cloud, which contributes to additional statistical fluctuations. A degradation of the energy resolution for this GPSC geometry is expected since for the same EL emission the number of VUV photons reaching the photosensor is much less than for other geometries where the photosensor is placed closer to the EL region. In addition, the fluctuations in the position where the EL amplification starts, at different distances from the anode surface, and the drift of the electrons in regions where the scintillation field is still weak also contribute to the overall statistical fluctuations of the scintillation pulses, like those occurring in proportional counters without a Frisch grid. This effect can be mitigated if waveform analysis of the scintillation pulses is implemented, e.g. as in [23, 24], accepting only waveforms with a time width within a selected time interval.

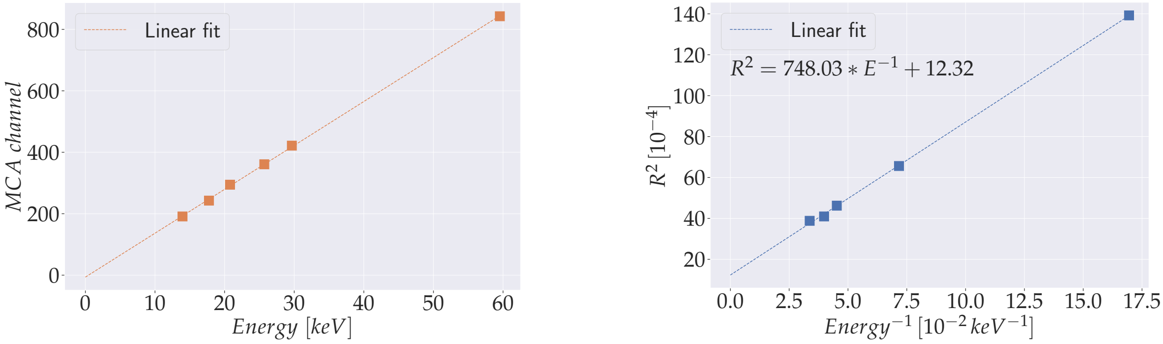

Figure 3. a) Pulse amplitude and b) square of the energy resolution as a function of the x-ray energy (E) and 1/E respectively, deposited in the GPSC.

Figure 4 shows both experimental and simulation results for the relative pulse amplitude and energy resolution obtained for 5.9 keV x-rays as a function of anode reduced voltage (V/p, where p is the Xe filling pressure). The energy resolution achieved for 10 kV anode bias is 12.0 % FWHM. The experimental results for the energy resolution are a little bit higher than those delivered by the simulations, which do not include the contribution of the statistical fluctuations introduced by the photosensor and other potential non-uniformities present in the detector. Electrical insulation is constraining the maximum voltage that can be applied to the anode in the present prototype. Simulations show that improved results can be obtained using higher biasing voltages. An energy resolution around 10 % is expected to be achieved for anode voltages around 13 kV.

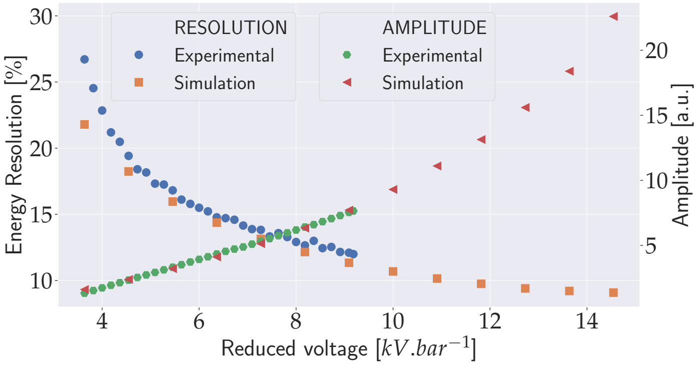

Figure 4. Pulse amplitude and energy resolution for 5.9 keV x-rays as a function of anode reduced voltage.

It should be noted that, in the present prototype, at high anode voltages, the regions around the PTFE wall have a reduced electric field above the Xe scintillation threshold, ~0.8 kV·cm^{-1}·bar^{-1} [24], due to the closer distance between the grounded chamber base plates (GPSC window and photosensor) and the anode. As referred to above, most of the EL takes place in the vicinity of the anode surface due to the radial dependence of the electric field in the region around the anode. Nevertheless, electron drift over longer paths in regions where the reduced electric field is above the scintillation threshold,

2025 JINST 20 C02021

but still weak, present higher EL statistical fluctuations due to the less efficient EL conversion [25]. In consequence, radiation interactions in the regions close to the detector wall will contribute to degrade the detector energy resolution in this prototype. For improved results, longer distances between the detector baseplates and the anode should be used to keep the reduced electric field at least near or below the scintillation threshold in those regions.

We substituted a large area avalanche photodiode (LAAPD) [13], having only 16-mm active diameter, for the 5-cm PMT. To limit the active diameter of the window, several collimators with different apertures were subsequently placed on top of the GPSC radiation window. In this way, we could test the EL pulse amplitude (integral) as a function of the GPSC active window diameter, for detector active window-to-photosensor diameter ratios above 2. Figure 5 presents these results for 10 kV bias in the anode and for 22.1 keV x-rays with the x-ray source placed at an increasing distance, h, to the detector window collimator, as depicted in figure 1, up to a maximum distance of 30 cm. As expected, the amplitude does not change with increasing active window diameter, denoting a constant solid angle subtended by the photosensor, independent from the x-ray interaction position. On the other hand, the energy resolution remains constant only up to active window diameters of ~5.5 cm, increasing for larger ones. This effect is explained in the above paragraph; since the x-ray beam is divergent the number of x-ray interactions occurring in the regions near the PTFE wall increases, leading to the degradation of the energy resolution.

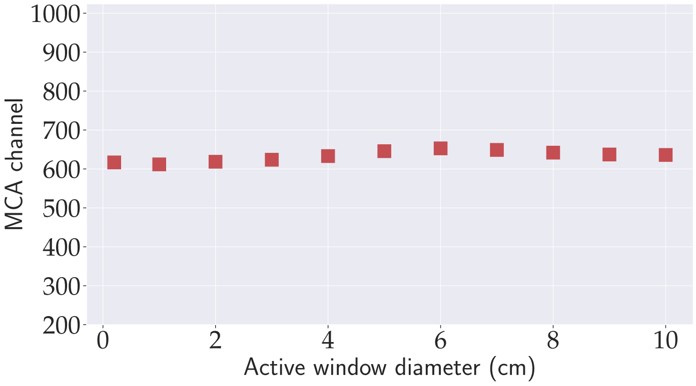

Figure 5. Pulse amplitude as a function of active window diameter for 22.1 keV x-rays.

Yet, a striking lesson should be drawn from the energy resolution value obtained with the LAAPD as the photosensor, which is 20–21% FWHM for 22.1 keV photons. In spite of the solid angle can be made constant even for large GPSC window-to-photosensor diameter ratios, this ratio cannot be made too large since one has to take into account the reduction on the solid angle subtended by the photosensor as the distance to the scintillation region increases, reducing the number of EL photons detected at the photosensor. This number has impact on the contribution of the statistical fluctuations of the photosensor to the overall energy resolution obtained in the GPSC. Simulation results show that the optical geometrical efficiency of EL detection by the photosensor, which includes not only the solid angle but also the photon reflections on the material surfaces, is one order of magnitude lower for the LAAPD photosensor case. This is the main reason for the energy resolution degradation from 6.8 to ~20% when replacing the PMT by the LAAPD. Therefore, it is mandatory to take into account the potential reduction of the solid angle subtended by the photosensor when considering the annular anode diameter.

5 Conclusions

A new very simple and robust design for a gas proportional scintillation counter aiming x- and γ-ray spectrometry applications is proposed. It uses one sole electrode, the anode, having an annular shape aligned with the axis of the photosensor. This design allows overcoming the constraints of the variation of the solid angle subtended by the photosensor relative to the different positions of the scintillation region, present in the standard GPSC designs with a parallel mesh geometry. It allows larger detection areas in comparison to the photosensor's sensitive area, without resorting to the complexity of electron focusing in the drift region or of non-uniform electric field in the scintillation region, proposed by former designs to mitigate the referred to above solid angle variations.

An energy resolution of 12.0 % FWHM is achieved for 5.9 keV x-rays in the present prototype, which features an anode with 10 cm inner diameter, biased at 10 kV, and a 5 cm diameter PMT placed 5 cm below the anode. According to simulations, an average number of 530 EL photons are produced per primary electron for an anode voltage of 10 kV, a value comparable to what is obtained in Xe at 1.1 bar, in a 1 cm thick uniform electric field close to the charge multiplication threshold, $4.5\,\mathrm{kV{\cdot}cm^{-1}{\cdot}bar^{-1}}$. The maximum voltage that could be applied to the anode without the presence of discharges was 10 kV. Nevertheless, simulations suggest that energy resolutions of ~10 % can be achieved for anode voltages around 13 kV, approaching the 9–10% values obtained by the geometries using solid angle variation compensation.

Effects such as photosensor and detector non-uniformities will contribute to the degradation of the detector energy resolution. A careful design of the detector should be implemented in order to minimize the drift regions where the reduced electric field is above the gas scintillation threshold.

Despite the full solid angle compensation demonstrated by the experimental results, a compromise must be made between the anode-to-photosensor diameter ratio, as well as between the anode-to-photosensor plane distance, and the energy resolution to be achieved in the detector. As the above ratio increases, the solid angle subtended by the photosensor decreases, leading to a decrease of the fraction of EL photons detected by the photosensor and to the increase of its corresponding stochastic statistical fluctuations. These fluctuations, if significant, lead to a degradation of the detector energy resolution.

Acknowledgments

This work was co-funded through national funds by FCT - Fundação para a Ciência e Tecnologia, IP within the framework of the projects LIBPhys UIDB/04559/2020 and UIDP/04559/2020.

References

[1] K. Koyama et al., *Performance verification of the gas scintillation proportional counters on board the TENMA satellite*, *Publ. Astron. Soc. Japan* **36** (1984) 659.

[2] A. Peacock et al., *The in-Orbit Performance of the Exosat Gas Scintillation Proportional Counter*, *IEEE Trans. Nucl. Sci.* **32** (1985) 108.

[3] P. Lamb et al., *The gas scintillation proportional counter in the Spacelab environment: in-flight performance and post-flight calibration*, *Astrophys. Space Sci.* **136** (1987) 369.

[4] D.F. Anderson, O.H. Bodine, R. Novick and R.S. Wolff, *A focusing gas scintillation proportional counter*, *Nucl. Instrum. Meth.* **144** (1977) 485.

[5] J.M.F. dos Santos et al., *Development of portable gas proportional scintillation counters for x-ray spectrometry*, *X Ray Spectrom.* **30** (2001) 373.

[6] H. Natal da Luz et al., *A large area gas proportional scintillation counter for balloon borne solar X-ray spectrometry*, *IEEE Trans. Nucl. Sci.* **49** (2002) 2488.

[7] C.A.N. Conde, *Gas proportional scintillation counters for X-ray spectrometry*, in *X-Ray Spectrometry: Recent Technological Advances*, K. Tsuji, J. Injuk and R. van Grieken eds., Wiley, New York, U.S.A. (2004), p. 195.

[8] S. Kobayashi et al., *A new generation γ-ray camera for planetary science applications: High pressure xenon time projection chamber*, *Adv. Space Res.* **37** (2006) 28.

[9] M. Mimura et al., *Xenon Time Projection Chamber for Next-Generation Planetary Missions*, *J. Phys. Soc. Jap.* **78** (2009) 157.

[10] D.A. Goganov and A.A. Schultz, *Performance of a gas electroluminescence x-ray detector filled with an argon-xenon mixture*, *Instrum. Exp. Tech.* **54** (2011) 409.

[11] A.S. Novikov et al., *New modification of xenon gamma-ray detector with high energy resolution*, *Opt. Eng.* **53** (2013) 021108.

[12] P.A.O.C. Silva et al., *A new concept for a gas proportional scintillation counter: the annular anode*, 2022 *JINST* **17** C05010.

[13] Advanced Photonix, a division of OSI optoelectronics, *Deep UV Large Area Avalanche Photodiodes (LAAPD)*, APX-SL2010APD-001.

[14] Salome, https://salome-platform.org/, Date accessed: October 28, 2024.

[15] Elmer-FEM, https://www.elmerfem.org/blog/, Date accessed: October 28, 2024.

[16] Paraview, https://www.paraview.org/, Date accessed: October 28, 2024.

[17] C.M.B. Monteiro et al., *Secondary Scintillation Yield in Pure Xenon*, 2007 *JINST* **2** P05001 [`physics/0702142`].

[18] GEANT4 collaboration, *Geant4 — A Simulation Toolkit*, *Nucl. Instrum. Meth. A* **506** (2003) 250.

[19] J. Allison et al., *Geant4 developments and applications*, *IEEE Trans. Nucl. Sci.* **53** (2006) 270.

[20] J. Allison et al., *Recent developments in Geant4*, *Nucl. Instrum. Meth. A* **835** (2016) 186.

[21] S. Biagi, *Transport of electrons in gas mixtures*, (2019), https://degrad.web.cern.ch/degrad/, Date accessed: October 28, 2024.

[22] H. Schindler and R. Veenhof, *Garfield++: simulation of ionisation based tracking detectors*, (2018), http://garfieldpp.web.cern.ch/garfieldpp, Date accessed: October 28, 2024.

[23] NEXT collaboration, *Neutral Bremsstrahlung Emission in Xenon Unveiled*, *Phys. Rev. X* **12** (2022) 021005 [`arXiv:2202.02614`].

[24] C.A.O. Henriques et al., *Understanding the xenon primary scintillation yield for cutting-edge rare event experiments*, *JCAP* **06** (2024) 041 [`arXiv:2309.14202`].

[25] F.P. Santos, T.H.V.T. Dias, A.D. Stauffer and C.A.N. Conde, *Three-dimensional Monte Carlo calculation of the VUV electroluminescence and other electron transport parameters in xenon*, *J. Phys. D* **27** (1994) 42.

[26] SAES st 707, https://www.saesgetters.com/products-functions/products/getters/non-evaporable-getters/pills-pieces, Date accessed: October 28, 2024.

2025 JINST 20 C02021